J Mater Sci (2009) 44:358–364
DOI 10.1007/s10853-008-3147-3

Synthesis, structural characterization, and photocatalytic properties of iron-doped TiO_2 aerogels

**M. Popa · L. Diamandescu · F. Vasiliu ·
C. M. Teodorescu · V. Cosoveanu · M. Baia ·
M. Feder · L. Baia · V. Danciu**

Received: 2 July 2008 / Accepted: 1 December 2008 / Published online: 16 December 2008

Abstract Fe(III)-doped TiO_2 aerogels are prepared by acid catalyzed sol–gel method followed by supercritical drying, and then heat treatment. Raman spectra together with X-ray diffraction (XRD) and selected area electron diffraction (SAED) patterns of the iron-doped TiO_2 aerogel samples revealed the existence of both anatase and brookite crystalline phases. It was found that the brookite phase formation is favored by the increase of the iron content in the dried samples. XRD measurements show that the lattice constant c of anatase phase decreases with the dopant addition, while the value of a remains essentially unchanged. The microstructure of the investigated samples is relatively compact with small mesopores as revealed from transmission electron microscopy (TEM). The most enhanced photocatalytic activity was exhibited by the TiO_2 aerogel sample with 1.8 at.% Fe(III) whose apparent rate constant of the salicylic acid photodegradation was found to be of almost six times higher than that of Degussa P25.

M. Popa · V. Cosoveanu · V. Danciu
Faculty of Chemistry and Chemical Engineering,
Babes-Bolyai University, 400028 Cluj-Napoca, Romania

L. Diamandescu · F. Vasiliu · C. M. Teodorescu · M. Feder
National Institute of Materials Physics, P.O. Box MG-7,
077125 Bucharest, Romania

M. Baia · L. Baia (✉)
Faculty of Physics, Babes-Bolyai University,
40084 Cluj-Napoca, Romania
e-mail: lucb@phys.ubbcluj.ro

Introduction

Photocatalysis using semiconductor materials has found increasing interest in solving environmental pollution problems [1–5].

Compared to other semiconductor photocatalysts, TiO_2 has so far been shown to be the most promising material used for both fundamental research and applications because it is highly photo-reactive, cheap, non-toxic, chemically and biologically inert, and photostable. A major drawback of TiO_2 is the large band gap of 3.2 eV, so wavelengths below 400 nm are necessary for excitation. This limits the photosensitivity to the UV part of the solar spectrum. In order to improve the quantum yield of TiO_2-based photocatalysis, the e^-–h^+ recombination rate needs to be reduced. For solving this problem, many efforts have been made and is generally accepted that there are three ways to achieve the separation of e^- and h^+: (a) by modifying TiO_2 by surface deposition of noble metal clusters [6–8]; (b) by coupling TiO_2 with other semiconductors possessing favorable band gaps and potentials like TiO_2–SnO_2 [9, 10]; (c) by introducing defects into the TiO_2 lattice by doping with transition metal ions [11–14].

Particularly, the photoactivity of the TiO_2 can be improved by means of Fe(III) doping [12–14] and by increasing its specific surface area through wet gel supercritical drying [15–18]. Fe(III)-doped TiO_2 has been synthesized via ‘‘wet’’ chemistry, i.e., hydrolysis of a Ti-precursor in the presence of a Fe(III)-containing aqueous solution or by mixing both Fe(III) and Ti(IV) precursors prior to hydrolysis [12–14].

In the present work, Fe(III)-doped TiO_2 aerogel photocatalysts with different iron doping content were prepared employing the acid catalyzed sol–gel method followed by low-temperature supercritical drying and thermal treatment.

The photocatalytic efficiency of these materials was evaluated by determining the apparent rate constants from the photodegradation process evaluation of the salicylic acid in aqueous solution. The main morpho-structural characteristics of the prepared Fe(III)-doped TiO_2 aerogels were analyzed by employing krypton adsorption, elemental analysis, and complementary techniques such as Raman spectroscopy, X-ray diffraction, TEM, and SAED.

Experimental

Sol–gel aerogel preparation

The acid catalyzed sol–gel process was carried out under normal conditions (760 mmHg, $T = 22$ °C). Two different solutions were prepared. A first solution contained 5 mL tetra-isopropyl orthotitanate—TIP (Merck, >98%) in 10 mL ethanol and a second one contained $Fe(NO_3)_3 \cdot 9H_2O$ (Aldrich) (0.25 M ethanolic solution), doubly distilled water ($V = 1.09$ mL), nitric acid and 10 mL ethanol. After homogenizing, the first solution was slowly added to the second one under vigorous stirring. The corresponding molar ratios are presented in Table 1. The resulted gels were covered and allowed to age for 6 weeks at room temperature. The ethanol was then removed by low-temperature supercritical drying with liquid CO_2 using a SAMDRI—PVT—3D dryer (Tousimis Res. Corp., USA). The obtained aerogels were calcinated at 773 K for 2 h in air, using a CARBOLITE furnace, and further characterized.

Photocatalytic activity

The photocatalytic activity of the Fe(III)-doped TiO_2 aerogels was determined by following the photodegradation of the salicylic acid (5×10^{-4} M) used as a test molecule. The initial ratio between salicylic acid and Fe(III)-doped TiO_2 photocatalyst was of 16.6 g aerogel/L. The organic compound was allowed to adsorb on the catalyst surface for 15 min in the dark, before UV irradiation. The salicylic acid concentration adsorbed on the catalyst surface was about 1.5–3.6% related to the initial salicylic acid concentration. Photodegradation profile was obtained from the concentration of salicylic acid measured with a Jasco V-530 spectrophotometer (from the decrease in the peak of 295 nm). The unchanged position of the adsorption peak of the spectrum could be explained by the aromatic ring opening that occurs in one step during the photocatalytic process (no other aromatic intermediates exist). To perform the spectroscopic measurements, the catalyst was separated from the salicylic acid solution by filtration, using a M.E. Cellulose 0.22 μm filter. Photodecomposition experiments were performed in a Teflon cell with a quartz window, for UV illumination using a 250 W high pressure Hg lamp. Irradiation intensity as measured with Eppley PSP Radiometer was 8 W/m^2. The photodecomposition reaction follows pseudo-first-order kinetics, consequently the apparent rate constant was calculated by plotting ln (C_0/C) versus time. The slope of the plot after applying a linear fit represents the apparent rate constant [19].

Morphological and structural characterization

Elemental analyses were performed with an inductively coupled plasma-mass spectroscope (ICP-MS). The Brunauer-Emmette-Teller (BET) surface areas (S_{BET}) were derived from krypton physisorption measurements at 77 K using a home-made glass installation. Prior to measurements, the samples were degassed to 0.001 Pa at 448 K. S_{BET} was calculated in the relative pressure range 0.05–0.3, assuming a cross-sectional area of 0.195 nm^2 for the krypton molecule. The measurement error by using krypton adsorption–desorption isotherms is only ±2 m^2/g (krypton molecule being smaller than nitrogen molecule).

The FT-Raman spectra of the investigated aerogel samples were recorded by using a Bruker Equinox 55 spectrometer with an integrated FRA 106 Raman module. A radiation of 1064 nm from a Nd-YAG laser was employed for excitation. The power incident on the sample was of 400 mW and the spectral resolution was of 1 cm^{-1}.

The structure of the aerogels was examined using a DRON X-ray powder diffractometer linked to a data acquisition and processing facility. CuK_α radiation ($\lambda = 1.540598$ Å) and a graphite monochromator were used.

A JEOL 200 CX TEM operating at an accelerating voltage of 200 kV was employed to obtain bright (BF) and

Table 1 Iron content, specific surface area (S_{BET}) and apparent rate constant for the Fe(III)-doped TiO_2 aerogels obtained in different molar ratio of the reactants, calcined at 773 K for 2 h

Sample	TIP:$Fe(NO_3)_3$:EtOH:H_2O:HNO_3 molar ratios	Fe (at.%)	S_{BET} (m^2/g)	$10^3 \times k_{app}$ (min^{-1})
A	1:0.030:19.22:3.57:0.113	1.8	163	14.9
B	1:0.015:17.95:3.57:0.113	0.9	141	13.1
C	1:0.0075:21.49:3.57:0.113	0.45	125	9.3
M (undoped TiO_2)	1:21.5:3.57:0.113	–	130	12.58
Degussa P25	–	–	50	2.5

dark (DF) field images as well as the electron diffraction patterns of the samples. Particle sizes were measured from BF and DF images, whereas the phase content was investigated by using electron diffraction patterns. Samples were prepared by dipping a 3 mm holey carbon grid into ultrasonic dispersed oxide powder in ethanol.

Results and discussion

The iron content and the specific surface area (S_{BET}) for the Fe(III)-doped TiO_2 aerogels obtained for different molar ratios of the reactants, calcined at 773 K for 2 h are listed in Table 1. It is remarkable that all TiO_2 aerogel samples have a specific surface area about three times greater than Degussa P25 powder. The highest specific surface area was obtained for the doped TiO_2 aerogels synthesized with a EtOH/TIP molar ratio of 19.22 with the highest iron content.

The apparent rate constants as function of time (Fig. 1), derived from the photodegradation process monitoring of the salicylic acid in the presence of the Fe(III)-doped TiO_2 aerogels, increase as the iron content becomes higher and are by four to six times greater than that of Degussa powder (see Table 1) [20]. The evolution of the apparent rate constant versus iron concentration is shown in Fig. 2. This result can be explained by their greater (two to three times) surface area and by the fact that Fe(III) centers form shallow charge trapping sites both within the TiO_2 matrix as well as on the particle surface through the replacement of Ti(IV) by Fe(III) [21]. Based on the favorable energy levels, Fe(III) centers may act either as an electron or a hole trap so that photogenerated charge carriers are temporarily separated more effectively than in undoped TiO_2. The photocatalytic efficiency is determined by the number of photogenerated charge carriers which can avoid the recombination reaction.

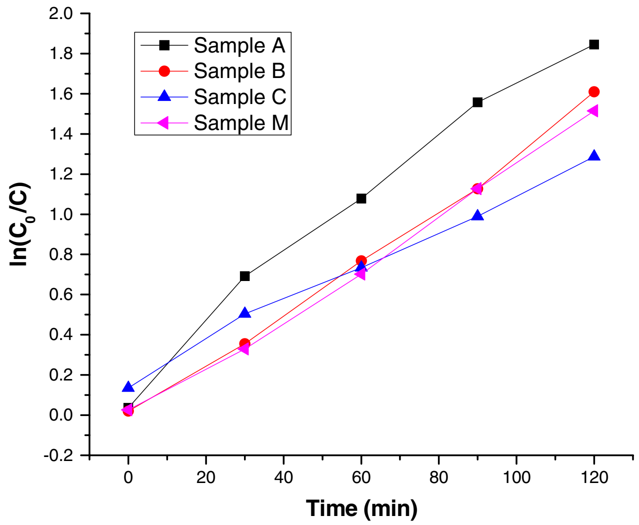

Fig. 1 Photocatalytic activity of the obtained photocatalysts

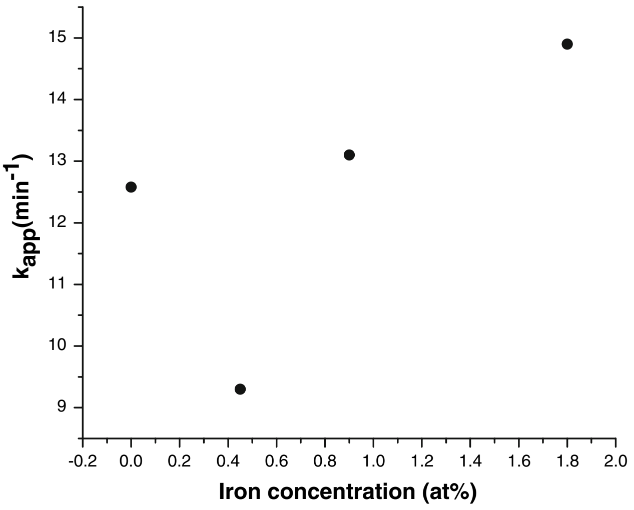

Fig. 2 Apparent rate constant evolution as function of iron content

Raman spectra recorded on the calcinated aerogels are shown in Fig. 3. As can be seen the Raman features recorded for all the samples can be associated mainly with those of the TiO_2 anatase crystalline phase. According to factor group analysis, the anatase phase gives rise to six Raman active modes ($A_{1g} + 2B_{1g} + 3E_g$) [22]. By inspecting the spectra one observes a strong sharp band at

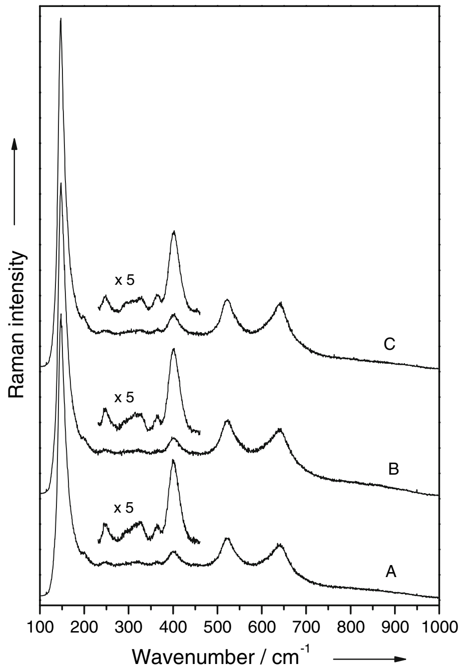

Fig. 3 Raman spectra of the iron-doped TiO_2 aerogels calcined at 773 K for 2 h, having different Fe(III) content: (A) 1.8, (B) 0.9, and (C) 0.45 at.% Fe

approximately 146 cm^{-1}, three medium intense bands around 396, 517, and 638 cm^{-1}, and a weak band at about 196 cm^{-1}. If we take into consideration the superimposition of two fundamental peaks near 517 cm^{-1} (Raman bands located at 515 and 519 cm^{-1}) these six peaks correspond to the six fundamental vibration modes of TiO_2 anatase with the symmetries E_g, E_g, B_{1g}, A_{1g}, B_{1g}, and E_g [22, 23]. However, a close analysis of the spectra reveals the appearance of other very weak Raman bands around 245, 320, and 365 cm^{-1} (see insets from Fig. 3). Such spectral features were previously observed, when ultrafine TiO_2 powders with grain sizes around 10 nm were investigated, and were attributed to the existence of a little amount of brookite phase [22–25]. It is worth mentioning that the brookite phase gives rise to 36 Raman active modes ($9A_{1g} + 9B_{1g} + 9B_{2g} + 9B_{3g}$), which are spread out on a wide spectral range, the most intense brookite Raman band occurring around 153 cm^{-1} [22, 26, 27].

In the last decades TiO_2 nanoparticles have been investigated with Raman spectroscopy because of the unusual broadening and shift of Raman bands with the change of the particles size, the most frequently spectral changes being related to the lowest frequency vibrational mode (146 cm^{-1}) [19, 28, 29]. Because numerous Raman features occur at almost the same wavenumbers for both anatase and brookite crystalline phases any correlation between the frequency and the half-width of the bands becomes very difficult. However, by comparing the ratios between the intensity of the band located around 400 cm^{-1}, which is given mainly by the anatase phase, and that of the band situated around 245 cm^{-1}, which is due to the brookite phase, a decrease of these values was found as the iron content increases. Thus, for 0.45 at.% Fe content a value of ~5.7 was obtained, while for the samples containing 0.90 and 1.80 at.% Fe the ratios were found to be of ~4.6 and ~4.4, respectively. This behavior demonstrates that the increase of the iron amount within the TiO_2 aerogel samples from 0.45 to 0.90 at.% Fe favors the brookite phase formation. The small variation observed for the two highest iron concentrations can be rigorously discussed only after a detailed analysis of these samples with other complementary techniques.

In order to get further insights into the structure of the iron containing aerogel samples X-ray diffraction measurements were performed and are presented in Fig. 4. X-ray diffraction patterns confirmed the major presence of the anatase phase accompanied by a rather significant fraction of brookite phase. Rietveld refinement (considering all peaks in the range of 20–70° (2θ)) reveals an increase of brookite phase (from 13% to 28%) as the iron content in the system increases (Table 2). The mean particle diameter of anatase phase is about 11 and ~9 nm for the brookite phase. In all cases c and a lattice parameters of anatase phase decrease by iron doping increase; both c and a parameters are lower than the values associated with undoped anatase suggesting the presence of Fe ions in the anatase lattice. If the a parameter is slightly changed (−0.2%), the axial parameter c decreases in the range with −0.62% till −1% (in comparison with the values of undoped phase, marked as sample M, in Tables 1 and 2) as the iron doping increases. The best-fit in the refinement runs was obtained considering a partial substitution of titanium by iron in the tetragonal anatase structure.

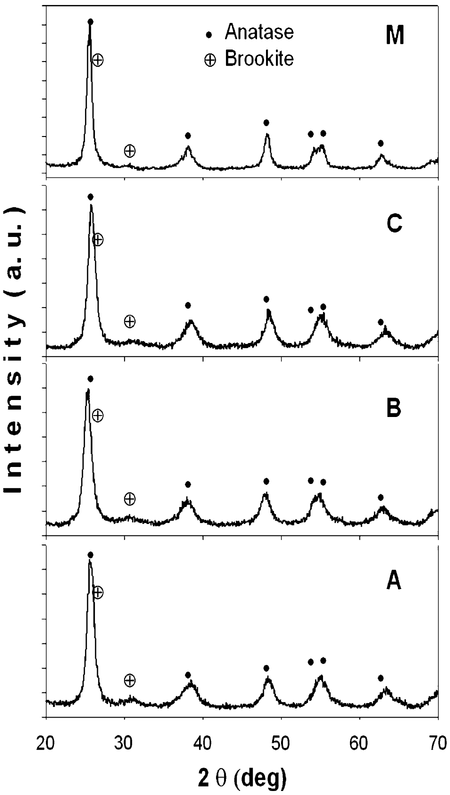

Fig. 4 X-ray diffraction patterns of the undoped (M) and iron-doped TiO_2 aerogels: (A) 1.8, (B) 0.9, and (C) 0.45 at.% Fe

From the data collected, one can infer that the lattice parameter c decreases with dopant addition, while the value of a parameter remains essentially unchanged. The anatase lattice was shown to deform predominantly along the c-axis to accommodate substitutionally incorporated Fe^{3+} because the effective ionic radii of Ti^{4+} and Fe^{3+} are 0.67 and 0.64 Å, respectively. Since only the axial parameter c is notably changing, while a remains the same, one can assume that Fe^{3+} substitutes Ti^{4+} preferentially on the body centered and face centered lattice sites in the anatase structure. This result, which must be confirmed by techniques such as extended X-ray absorption fine structure (EXAFS), is very important since it suggests that substitutive dopants can act directly as trapping sites to enhance the carrier lifetime.

Table 2 Rietveld refinement parameters (phase contents, mean particle size, and lattice parameters) determined from XRD spectra

Sample	Phase content (%)		Mean particle size (nm)		Lattice parameters (Å)	
	Anatase	Brookite	Anatase	Brookite	*a*	*c*
A	72.1	27.9	12	9	3.7820 (5)	9.4417 (6)
B	72.1	27.9	11	9	3.7907 (6)	9.4508 (4)
C	82.8	17.2	11	9	3.7923 (4)	9.4773 (5)
M	86.5	13.5	18	11	3.7925 (3)	9.5075 (4)
Errors	±0.8	±0.8	±1	±1		

TEM images of the specimens exhibit mainly Fe(III)-doped TiO_2 nanoparticles having diameters between 8 and 12 nm (the mean size is about 10 nm) (Fig. 5a–c). The average TiO_2 particle diameter thus obtained from the TEM analysis is close to the value estimated from the broadening of X-ray diffraction lines. The size distribution is monomodal excepting the specimen with the lowest Fe content which exhibits a bimodal distribution (Fig. 6). Generally, only mesoropores having sizes between 10 and 30 nm were observed and the minimal size of detected pores was similar to the mean size of anatase nanoparticles. The porosity can be changed as a function of iron doping. Thus, in the sample C (Fig. 5a), which has a minimal iron content, a high and interconnecting porosity was detected, while the sample B (Fig. 5b), which is very compact, contains a major fraction of individual pores, without intercommunication among them. A peculiar structure is registered for the highest iron content sample (Fig. 5c) where the microporosity was found to increase; a circumferential and interconnecting porosity around anatase particles can be observed in the inset of Fig. 5c. The structural information given by SAED is in good agreement with X-ray diffraction data. The presence of brookite phase besides the major anatase phase (Fig. 3d) leads to a broadening of the strongest ring (101) of the anatase phase, which is overlapped with the line (111) ($I = 80$) of the brookite. A strong diffuse ring (121) of the brookite is observed at $d = 2.90$ Å between the successive (101) and (200) anatase rings. SAED patterns confirmed the decrease of the axial lattice parameter *c* as the iron content increases.

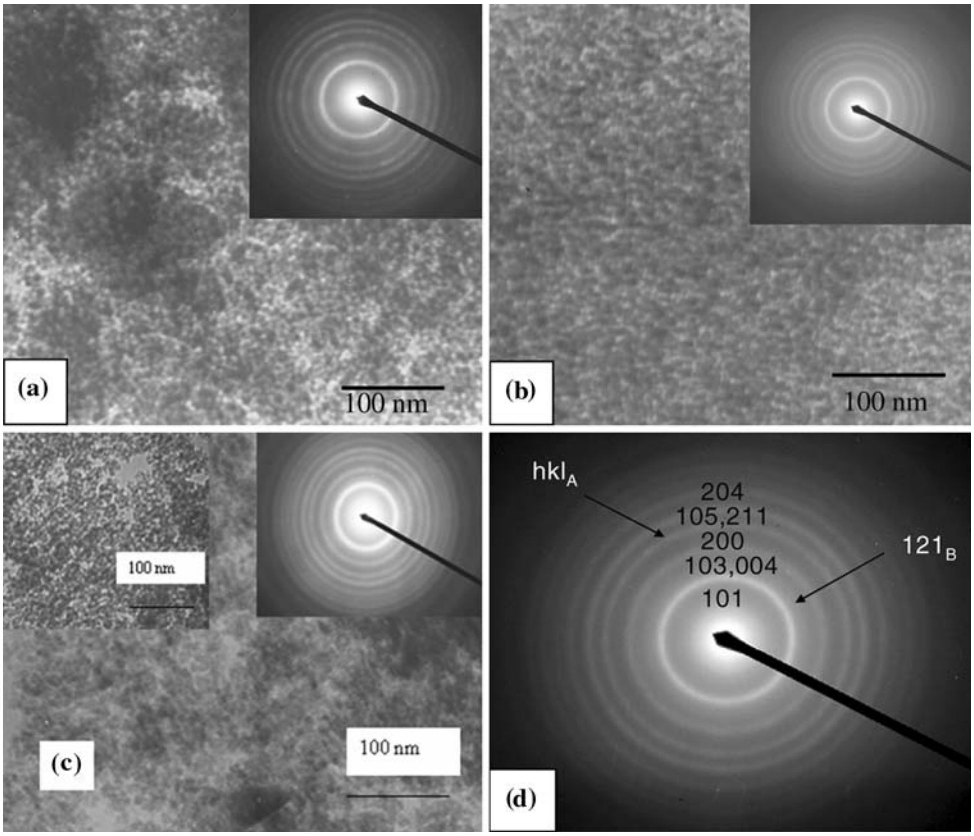

Fig. 5 TEM images and SAED patterns associated to specimens having different Fe(III) content: **a** 0.45 at.% Fe (sample C); **b** 0.9 at.% Fe (sample B); **c** 1.8 at.% Fe (sample A); **d** an indexed SAED pattern of well-crystallized anatase particles (where *hkl*$_A$—anatase diffraction rings and 121_B—brookite diffraction ring)

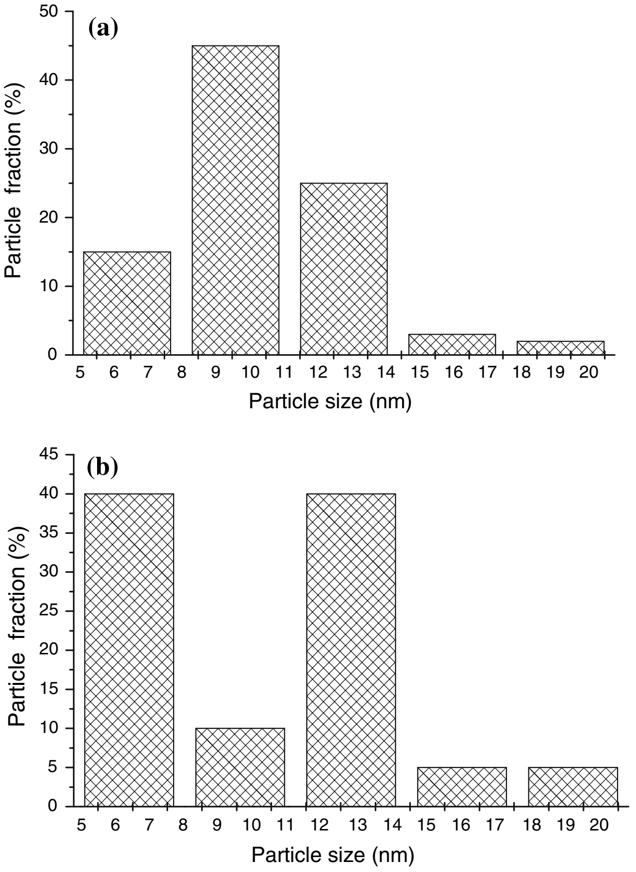

Fig. 6 The particle size distribution for Fe-doped TiO_2 aerogels: **a** specimen A and **b** specimen C

Conclusions

Fe(III)-doped TiO_2 aerogels with specific surface areas of up to 151 m^2/g were prepared using the acid catalyzed sol–gel method followed by low-temperature supercritical drying and heat treatment. Varying the ethanol-to-titania precursor and the $Fe(NO_3)_3$-to-titania precursor molar ratios and applying the low-temperature supercritical drying for the removal of the solvent entrapped in the porous gels network, resulted in aerogels with different morphological properties. Increasing the ethanol-to-titania precursor ratio, from 17.95 to 21.49 resulted in a larger specific surface area. The iron-doped TiO_2 aerogel with the highest content (1.8 at.%) has the highest photoactivity, although it has the maximum brookite content. Shallow trapping of the photoelectron by Fe(III) followed by rapid iron-catalyzed transfer of the electron to adsorbed molecule is suggested as a tentative explanation for the enhancement of photocatalytic activity.

Raman spectra of the iron-doped TiO_2 aerogel samples revealed the existence of both anatase and brookite crystalline phases. It was found that the brookite phase formation is favored by the increase of the iron content in the calcined samples. The microstructure of the samples investigated by TEM shows a relatively compact microstructure with small mesopores (individual and non-communicating). The porosity varies as a function of the iron content and the increasing doping leads to an important decrease of pore size and interconnectivity. Both X-ray diffraction and SAED patterns revealed a major anatase phase mixed with a brookite fraction. X-ray diffraction measurements show that the lattice parameter c of anatase phase decreases with dopant addition, while the value of a remains essentially unchanged. It can be presumed that Fe^{3+} substitutes Ti^{4+} preferentially on the body centered and face centered lattice sites in the anatase structure, since only the axial parameter c changes, while a remains the same. This result is very important for photocatalytic activity since only substitutive dopants can act directly as trapping sites to enhance the carrier lifetime. Thus, the as obtained Fe(III)-doped titania aerogels are interesting catalysts for environmentally imperative applications.

References

1. Bahnemann D, Cunningham J, Fox MA, Pelizzetti E, Serpone N (1994) In: Helz GR, Zepp RG, Crosby DG (eds) Aquatic and surface photochemistry. Lewis Publisher, Boca Raton, FL
2. Ollis DF, Al-Ekabi H (1993) Photocatalytic purification and treatment of water and air. Elsevier, Amsterdam
3. Hoffmann MR, Martin ST, Choi W, Bahnemann DW (1995) Chem Rev 95:69
4. Pichat P (1994) Catal Today 19:313
5. Wang C-Y, Liu C-Y, Shen T (1997) J Photochem Photobiol A 109:65
6. Wang C-Y, Liu C-Y (2002) In: Hubbard A, Barbara S (eds) Encyclopedia of surface and colloid science. Marcel Dekker, NY, p 4926
7. Wang C-Y, Liu C-Y, Zheng X, Chen J, Shen T (1998) Colloids Surf A 131(1–3):271
8. Wang C-Y, Liu C-Y, Chen J, Shen T (1997) J Colloid Interf Sci 191:464
9. Cao Y, Zhang X, Yang W, Du H, Bai Y, Li T, Yao J (2000) Chem Mater 12:3445
10. Tada H, Hattori A, Tokihisa Y, Imai K, Tohge N, Ito S (2000) J Phys Chem B 104:4585
11. Wang C-Y, Bahnemann D, Dohrmann JK (2000) Chem Commun 1539
12. Wang JA, Limas-Ballesteros R, Lopez T, Moreno A, Gomez R, Novaro O, Bokhimi X (2001) J Phys Chem B 105:9692
13. Barau (Szatvanyi) A, Crisan M, Gartner M, Danciu V, Cosoveanu V, Marian I, Anastasescu M, Zaharescu M (2005) Mat Sci Forum 492–493:311
14. Barau (Szatvanyi) A, Crisan M, Gartner M, Jitianu A, Zaharescu M, Ghita A, Danciu V, Cosoveanu V, Marian I (2006) J Sol-Gel Sci Tech 37:175
15. Kelly S, Pollak FH, Tomkiewicz M (1997) J Phys Chem B 101:273
16. Zhu Z, Lin M, Dagan G, Tomkiewicz M (1995) J Phys Chem 99:15953

17. Peter A, Danciu V, Cosoveanu V, Moldovan Z, Indrea E, Nutiu G, Baia L, Rosu I (2005) In: Proceedings of innovations in the field of water supply sanitation and water quality management, p 103
18. Wang C-Y, Bottcher C, Bahnemann DW, Dohrmann JK (2003) J Mat Chem 13:2322
19. Baia L, Baia M, Peter A, Cosoveanu V, Danciu V (2007) J Optoelectr Adv Mater 9(3):668
20. Ryu J, Choi W (2008) Environ Sci Technol 42:294–300
21. Ohsaka T, Izumi F, Fujiki Y (1978) J Raman Spectrosc 7:321
22. Adan C, Bahamonde A, Fernandez-Garcia M, Martinez-Arias A (2007) Appl Catal B Environ 72:11–17
23. Zhang YH, Chan CK, Porter JF, Guo W (1998) J Mater Res 13:2602
24. Busca G, Ramis G, Amores JMG, Escribano VS, Piaggio P (1994) J Chem Soc Faraday Trans 90:3181
25. Gotic M, Ivanda M, Sekulic A, Music S, Popovic S, Turkovic A, Furic K (1996) Mater Lett 28:225
26. Tompsett GA, Bowmaker GA, Cooney BP, Metson JB, Rodgers KA, Seakins JM (1995) J Raman Spectrosc 26:57
27. Kelly S, Pollak FH, Tomkiewicz M (1997) J Phys Chem B 101:2730
28. Baia L, Peter A, Cosoveanu V, Indrea E, Baia M, Popp J, Danciu V (2006) Thin Solid Films 511–512:512
29. Choi HC, Jung YM, Kim SB (2005) Vibrat Spectrosc 37:33